Monthly Notices of the ROYAL ASTRONOMICAL SOCIETY

MNRAS **541,** 3320–3330 (2025) https://doi.org/10.1093/mnras/staf1163
Advance Access publication 2025 July 16

Variations of the Ca II K line profile parameters with solar latitude and time observed from Kodaikanal Solar Observatory

Apoorva Srinivasa [1★] Anu Sreedevi,[2] K. P. Raju [3] K. Nagaraju,[3] Jagdev Singh,[3] Narayanankutty Karuppath,[1] P. Devendran,[4] T. Ramesh Kumar[4] and P. Kumaravel[4]

[1]*Department of Physics, Amrita Vishwa Vidyapeetham, Amritapuri, 690525, India*
[2]*Department of Physics, Indian Institute of Technology (Banaras Hindu University), Varanasi, 221005, India*
[3]*Indian Institute of Astrophysics, Koramangala, Bengaluru, 560034, India*
[4]*Indian Institute of Astrophysics, Kodaikanal, 624103, India*

Accepted 2025 July 14. Received 2025 July 8; in original form 2024 November 14

ABSTRACT

The Ca-K line profiles as functions of solar latitude and time were obtained through our observations from the Kodaikanal Solar Observatory using the solar tunnel telescope and spectrograph with a CCD detector. Observations were conducted on all days with favourable sky conditions. We analysed the data collected over a period of about 10 yr to study the variations in the Ca II K line profiles recorded between 2015 and 2024, of which 709 d of data were found useful. The temporal and time-averaged latitudinal variations of the K_1 width, K_2 width, K_3 intensity and the intensity ratios of K_{2v}/K_{2r} and K_{2v}/K_3 were computed using a semi-automated program. The parameters showed asymmetric increases towards the higher latitudes, with the rates of increase being higher in the Southern hemisphere. The temporal plots for K_1 width and K_3 intensity showed positive correlations with the plage and spot filling factors, whereas the temporal plots for K_2 width, K_{2v}/K_{2r}, and K_{2v}/K_3 intensity ratios showed negative correlations. The time-averaged latitudinal plot for K_1 width has small peaks near 25°N and 20°S. The K_2 width has a small peak at 0°. The K_3 intensity has peaks at 20°N and 15°S. The K_{2v}/K_{2r} intensity ratio shows peaks at 50°N, 0°, and 40°S. The K_{2v}/K_3 intensity ratio shows peaks at 60°N, 0°, and 60°S. Slope profiles show spectral response to magnetic activity peaks near K_3 with north–south asymmetries. Such variations in the line profiles are important in the studies of solar irradiance, surface flux transport, and solar dynamo.

Key words: dynamo – Sun: activity – Sun: atmosphere – Sun: chromosphere.

1 INTRODUCTION

The variability of the Sun's magnetic field and radiative output significantly impacts not only solar phenomena but also terrestrial climate and space weather. These variations span a wide range of time-scales, from short-term (seconds) to long-term (years) processes (Gray et al. 2010). The short-term variations include granulation life (several minutes), sunspot movements (few days), and faculae (few days to weeks). The long-term variations include the solar cycle (∼11 yr) and solar irradiance. Several indices and parameters – solar radio flux, solar irradiance, ultraviolet index, Ca-K emission index, and geomagnetic indices – are used to understand and quantify solar variability (Hathaway 2015).

About 63 per cent of the variation in the total solar irradiance occurs in the UV part of the solar spectrum (Morrill, Floyd & McMullin 2011). Although only 1 per cent of electromagnetic radiation comes from the Sun at wavelengths smaller than 300 nm, it may contribute more than that to the variations in total irradiance. The fluctuation resulting from large sunspot regions offsets the change in solar irradiance induced by the bright faculae (Froehlich et al. 1991; Pap et al. 1997). The understanding of how different features, including plages, networks, sunspots, and others, contribute to irradiance variability has advanced significantly in the last few years (Solanki, Krivova & Haigh 2013). Over the course of the 11-yr solar cycle, the Ca-K index fluctuates by 18 per cent (White & Livingston 1981). The fluctuation in total irradiance caused by a solar cycle has an amplitude of 0.1 per cent (Fröhlich & Lean 1998). The correlation between the magnetic field of the sun and Ca-K emission makes spectroscopic investigation of the solar chromosphere important (Nindos & Zirin 1998; Ortiz & Rast 2005).

The solar magnetic field, generated by the solar dynamo, drives much of the sun's activity. Understanding this magnetic field's evolution is essential to studying solar activity cycles and their impact on solar irradiance. A key component of the solar dynamo is the migration of the sunspot regions to the solar equator (Charbonneau 2020; Makarov & Tlatov 2000). The variation in Ca-K line profiles across latitudes suggests that magnetic flux transfer takes place on the surface of the sun (Sindhuja, Singh & Ravindra 2014). It may be noted that the canopy effect and geometrical foreshortening affect the measurements made above 75° latitude, causing poor approximation of the flux distribution (Worden & Harvey 2000). The variations in Ca-K line profiles are mainly caused by plages and chromospheric networks (Cretignier, Pietrow & Aigrain 2024). The temporal variation of the strength of the underlying magnetic field

★ E-mail: ampsr4phy22001@am.students.amrita.edu

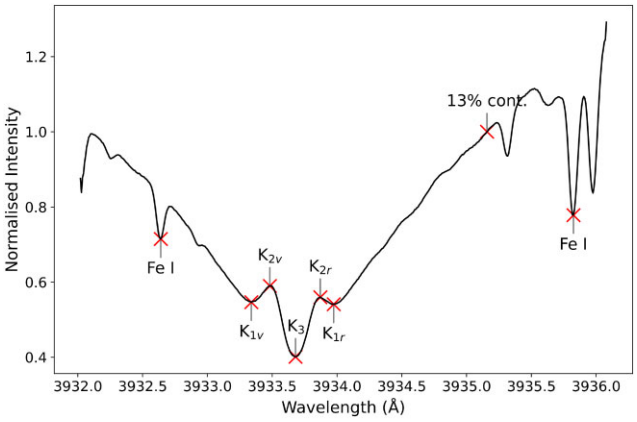

Figure 1. A typical Ca-K line profile from our observations. The three principal features (K_1, K_2, and K_3) of the profiles are marked.

primarily contributes to the differences in intensities of distinct Ca-K plages, which may also vary throughout different phases of the solar cycle (Sindhuja & Singh 2015).

The calcium line was first detected by Joseph Fraunhofer in 1814, and it was included as K in his list of prominent absorption features. Hale & Ellerman (1904) introduced designations for three parts of the Ca-K line profiles. These are shown in Fig. 1, which is an example of a typical Ca-K line profile from our observations. In the figure, the central absorption is called K_3. The emission features on either side of K_3 are K_{2v} and K_{2r}, and the minima in the profile wings beyond the emission peaks are K_{1v} and K_{1r}. The wavelength difference between K_{2v} and K_{2r} is the K_2 width, and the difference between K_{1v} and K_{1r} is the K_1 width. The source function – the ratio of the emission coefficient to the absorption coefficient – for the K line reflects the value of the local temperature of the region (Vernazza, Avrett & Loeser 1981). The increase in temperature results in an increase in source function. At about 1900 km, higher temperatures result in an increased population of ionized calcium atoms. These ionized calcium atoms effectively absorb radiation at the specific wavelength corresponding to the calcium-K line, leading to the formation of the dark core reversal (K_3) ≈1700–2000 km from the solar surface. At lower heights, the source function is affected by scattering due to lower temperatures, thus contributing to the formation of wings (K_1 minima) ≈400–600 km. This mechanism causes the existence of two bumps in the line profile near its core (K_2 peaks), at ≈700–1500 km. The Ca-K line is particularly interesting to solar astronomers studying solar variability because it provides information about the activity and dynamics of the sun's chromosphere (Sivaraman et al. 1987).

It was observed that the Ca-K line profiles change with the solar cycle (White & Livingston 1978; Oranje 1983; Bertello, Pevtsov & Ulrich 2020). From the spatially resolved spectra, it was found that the areas of plages and networks exhibit larger K_1 widths and smaller K_2 widths when compared to those of quiet regions (Bappu & Sivaraman 1971; White & Livingston 1981). In general, it was found that K_{2v} has a larger intensity than K_{2r}. The lifespan of sunspots influences the K_1 and K_2 widths (Chatzistergos, Krivova & Ermolli 2022), which in turn reflect the extent to which the area and intensity of features vary every day. These variations in K_1 and K_2 widths, as well as the intensities at the wavelengths of these emission peaks and wings, provide valuable insights into the magnetic activity occurring in solar plages and networks, important features that influence the solar cycle's impact on solar irradiance (Sindhuja & Singh 2015). In order to study limb darkening, K_2 widths as a function of longitude have been analysed by Engvold (1966).

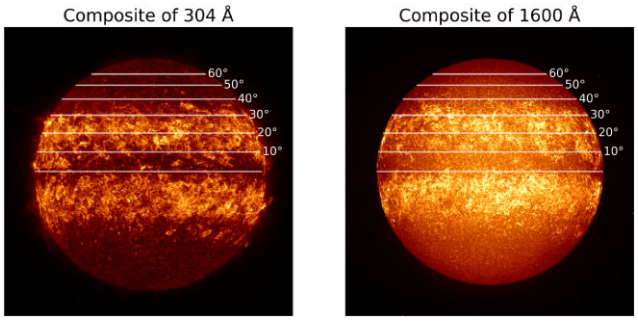

Figure 2. Composite images of the sun at 304 Å (left) and 1600 Å (right) constructed from the data overlapping with our observation days. (Original data are courtesy of SDO's AIA).

Since 1969, the sun-as-a-star observations in the chromospheric Ca-K line have been conducted at the Kodaikanal Solar Observatory (KSO; lat. 10°14′ N; long. 77°28′ E). From 1969 to 1984, the changes in Ca-K line parameters with the solar cycle were studied by using the solar disc-averaged Ca-K line profiles (Sivaraman et al. 1987). Since 1986, chromospheric variations with both the solar cycle and latitude have been analysed using Ca-K spectra acquired as a function of latitude and integrated over longitudes by Singh (1988). By isolating the contributions of plages and networks, the study was able to more accurately assess the variability in the Ca-K line width. This methodology of integrating spectra over visible longitudes at specific latitude belts was developed primarily to study the temporal variations of chromospheric activity as a function of solar latitude over extended periods, covering multiple solar cycles. While local line formation physics depends on parameters such as surface element velocity and centre-to-limb angle (Lagg et al. 2017; Cretignier et al. 2024), the latitude-resolved approach offers unique advantages for tracking large-scale solar dynamics. The relationships between the different coordinate variables (line-of-sight velocity, centre-to-limb angle, and latitude) are presented in Appendix A.

Fig. 2 shows composite images from the Solar Dynamics Observatory's (SDO) Atmospheric Imaging Assembly (AIA) at 304 and 1600 Å. We constructed these composites from over 100 individual AIA images (from 2023 and 2024) acquired during our observation period using the max stacking method. This method records the maximum value at each pixel from all the images in the pool and generates the composite image. As can be seen from the composite images, the activity regions are concentrated between 40°N and 40°S. A Butterfly-diagram-like pattern is visible in the composites of both 304 and 1600 Å.

The latitude-wise (LW) analysis with longitude integration provides valuable insights into the distribution and evolution of magnetic activity across solar latitudes over time. While our Ca-K line parameters are intensity metrics rather than direct velocity measurements, they serve as effective tracers of magnetic features (plages, enhanced network) that are passively transported by large-scale plasma flows. Meridional circulation, characterized by polewards flows at the surface and equatorwards return flows in the interior (Priyal et al. 2023), is known to transport magnetic flux as part of the solar dynamo mechanism. By analysing the systematic latitudinal migration of magnetic activity through our Ca-K intensity proxies, we can identify patterns consistent with the transport effects of meridional flows. This approach allows us to observe the consequential signatures of these flows rather than measuring the flows themselves, providing indirect

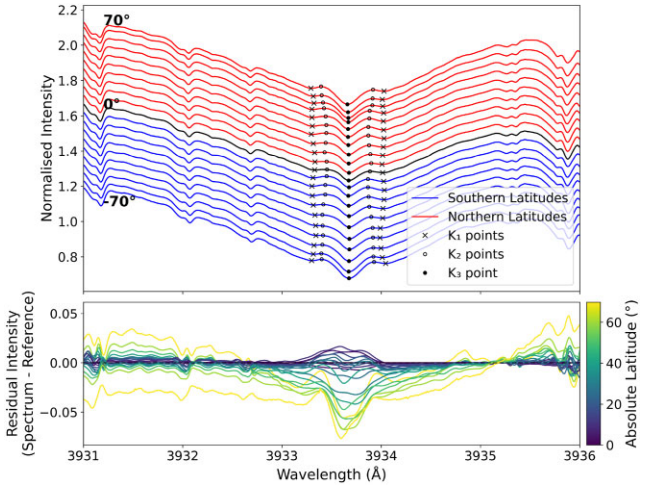

Figure 3. Top: LW Ca-K line profiles from our observations. Starting from −70°, the profiles are successively offset vertically by 0.05 units for visual clarity. Bottom: residual intensity plot of the profiles taking the profile at the equator as the reference.

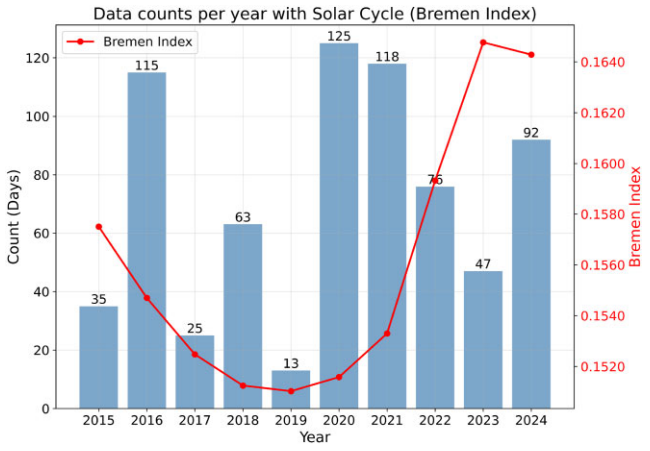

Figure 4. Bar chart showing the spread of our data over 2015 to 2024. The solar irradiance variability over the years is shown by the Bremen composite Mg II index or Bremen Index (Snow et al.2014).

evidence of their influence on magnetic feature distribution across different latitudes in both hemispheres. Such observations contribute to our understanding of the transport mechanisms involved in solar dynamo processes (Sindhuja et al. 2014). Extensive studies have been conducted on the fluctuations of Ca-K line profiles as functions of latitude and time during solar cycles 22 and 23 by Sindhuja (2015). The study included in-depth analyses of the meridional flow patterns using the Ca-K line profiles, providing valuable insights into the mechanism of the solar dynamo. Fig. 3 shows the Ca-K line profiles plotted for several latitudes to illustrate the variations across latitudes. The figure also includes a residual plot made using the equator profile as the reference. It shows that the intensities at higher latitudes are lower than those of lower latitudes at the core of the profiles.

While our method is not directly designed to study differential rotation (where different latitudes rotate at different speeds), the latitude-dependent evolution of chromospheric features tracked through Ca-K emission can indirectly reflect aspects of differential rotation (Keil & Worden 1984; Bertello et al. 2020). Similarly, though we do not resolve individual granules or supergranules, the cumulative effects of granular and supergranular convection and diffusion influence the transport and distribution of magnetic flux observed in the chromospheric network through Ca-K emission (Worden & Harvey 2000; Norton, Charbonneau & Passos 2014). By obtaining a statistical average of chromospheric conditions at different latitude belts through longitude integration, we reduce the impact of localized short-lived features and focus on longer term latitude-dependent trends relevant to the solar dynamo.

Our study extends the analysis of chromospheric variations by examining solar cycle-dependent changes in the Ca-K line profiles obtained for a period of about 10 yr, from 2015 to 2024, and contains 709 d of useful data (Fig. 4) to examine the variation of Ca-K line parameters as functions of latitude and time. In Section 2, we provide the details of the observations from the KSO and the methodology used for getting the data ready for analysis, followed by a list of parameters used for data analysis. Sections 3, 4, and 5 detail the results obtained, the discussions on those and conclusions.

2 OBSERVATIONS AND DATA ANALYSIS

2.1 Observations

The longitudinally integrated Ca-K spectra have been recorded at KSO as a function of solar latitude since 1986 (Singh 1988). The spectra were recorded using a CCD camera of 2K × 2K format with a pixel size of 13.5 × 13.5 microns. The image scale on this detector is 0.07 arcsec pixel^{-1}, the spectral sampling is 5.6 mÅ pixel^{-1}, and the spectral resolution (limited by the 100 μm slit width) is approximately 11 mÅ, giving an equivalent R of ≈350 000. The observations are carried out during the morning hours due to the better seeing conditions and require a cloud-free sky for about 45 min. This is to minimize atmospheric turbulence and ensure optimal image quality during acquisition. The observing days are mostly confined to the months between September and March and occasionally a few days from April to August as the other days are affected by the south-west and north-east monsoons in Kodaikanal.

We have adopted Sindhuja (2015)'s imaging method of the sun's spectra – improved upon (Singh 1988) – around the Ca-K line wavelength as a function of latitude integrated across longitude as follows:

(i) Sun charts are made considering the size of the sun's image and proper ephemerides (such as the inclination of the sun or B_0 angle) such that the centre of the chart is located at the B_0 angle.

(ii) The sun chart is set up such that its marked north–south axis is parallel to the sun's image's rotation axis.

(iii) A fraction of the sun's image is allowed to pass through the spectrograph's slit in such a way that when the North limb of the sun's image moves along a latitude line, the same latitude falls on the slit centre.

(iv) To get the Ca-K wavelength spectra, the sun's image is moved uniformly from its east to west end on the spectrograph's slit at specific latitudes.

(v) The widths of the latitude belts taken are 10° in ±(30°–70°) and 5° in (0°–±30°).

2.2 Calculation of profile parameters

The data were corrected for dark and flat field variations. We developed a semi-automated program to perform the following:

(i) A slice from any spectral image shows us the line spectrum. In order to deal with some of the noise or artefacts that may have slipped the corrections, from each data file, we considered around 300–350 slices to obtain the averaged spectra for that particular latitude.

(ii) For the wavelength calibration, the photospheric absorption lines of Fe I (shown in 1) at 3932.640 and 3935.825 Å were used. Rough windows were specified around these points and fitting algorithms were used within the windows to extract the exact positions of these points automatically.

(iii) To normalize the widely varying intensity values, we used the residual intensity value (13 per cent of the continuum as determined by White & Suemoto (1968) at 3935.160 Å (shown in 1) to scale the intensity values in each spectrum.

(iv) We extracted most of the data points automatically using fitting algorithms. Those data points that had values that went beyond the tolerance set in the algorithms were extracted by locating the points manually.

(v) Lastly, we removed the outliers by considering the 2σ-window for each year.

The parameters of the Ca-K line profiles analysed in this study are K_1 width, K_2 width, K_3 intensity, K_{2v}/K_{2r} intensity ratio and K_{2v}/K_3 intensity ratio.

2.3 Calculation of spot and plage filling factors

To investigate the relationship between Ca-K line profile parameters and solar activity features, we calculated the spot and plage filling factors (FFs) using the SolAster package (Ervin et al. 2022) for the days corresponding to our Ca-K observations. We utilized the Helioseismic and Magnetic Imager (HMI) data from the SDO for the period from 2015 to 2024, which covers the majority of our observational period. For each day of our Ca-K observations, the corresponding SDO/HMI images were retrieved and processed to calculate the sun-as-a-star [or disc-integrated (DI)] plage + spot FF as well as LW FF. Since the spot FF tend towards 0 beyond $\pm 40^\circ$ latitudes, where minimal spot activity is observed, we decided to consider (plage + spot) FF for our analyses.

The relationship between the calculated FF and the Ca-K line profile parameters was then assessed through correlation analysis to identify possible connections between photospheric/chromospheric features and the spectral characteristics observed in our study. This analysis complements the traditional sunspot number correlation and provides additional insights into how different magnetic features contribute to the observed spectral variations (Sivaraman et al. 1987; Cretignier et al. 2024).

2.4 Calculation of flux difference per FF difference

To investigate the activity profile per unit of FF at the mean μ angle, we did the following:

(i) Extracted the quiet sun latitude profiles for each of the latitudes by considering only those days in 2020 when zero sunspots were reported. These profiles were averaged LW to obtain the reference profiles.

(ii) From each day's profiles from our time period, we differenced the reference profiles LW to obtain the 'corrected' profiles.

(iii) Next, we performed similar steps with FF data, again, LW and considered (plage + spot) FF.

(iv) With these data in hand, we considered a 1.2 Å window around 3933.6 Å to calculate the flux difference per FF difference at each wavelength point in the selected window.

(v) A linear fit was performed between the time series of flux differences and the time series of FF differences.

(vi) The slope coefficients obtained were plotted against the corresponding wavelengths at which they were obtained.

2.5 Sources of uncertainty

Observational data inherently contain uncertainties. The possible sources of uncertainty in our data include the following:

(i) Environmental factors such as atmospheric distortions, air-mass, and weather variability may have affected the data collected.

(ii) CCD degradation over time due to pixel defects, declining charge transfer efficiency, etc. may have resulted in small errors.

(iii) The correction data collected for dark currents and flat fields may not have removed the noise and artefacts completely.

(iv) Since the data extraction was done using fitting, there may have been minor inaccuracies due to imperfect fits.

(v) Manual location and extraction of data points may have contributed to errors due to the presence of human elements.

3 RESULTS

After computing the above-mentioned parameters from the data for each day of observations, we describe their variations as functions of time and solar latitude in the following subsections. Temporal variation plots are shown along with the FF data for the selected time period between 2015 August and 2024 April. The time-averaged LW measurements – their mean and standard deviation ranges – for each parameter are summarized in Table 1.

3.1 Variations in K_1 widths

Fig. 5 shows the variations in the K_1 widths over time for select latitudes. Each of the latitudes plotted (except 60°S) shows a similar underlying trend, which is a decrease in the widths during 2015–2019/2020, followed by an increase towards 2024. The trend for 60°S shows only an increase during 2015–2024. The Pearson correlation coefficients (CCs) between the K_1 width and LW-FF as well as DI-FF are positive. The maximum LW- and DI-FF correlations of 0.99 and 0.94 are obtained at the 20°S and 20°N latitudes, and minimum correlations of 0.18 and 0.36, both are obtained at 60°S.

Fig. 6 shows the plot of K_1 width, averaged over time, as a function of latitude. The width varies in the range of 0.591–0.739 Å, with the standard deviations ranging from 0.029 to 0.060 Å. The figure shows that the K_1 width generally increases with the latitude in both hemispheres. The K_1 width shows larger values around 20–25°N and 20°S compared to the values for the previous neighbouring latitudes. The widths are generally larger in the Southern hemisphere, and their increase is steeper in the Southern hemisphere, moving from 40°S to 70°S. The averaged K_1 width over all latitudes varies by 34.42 per cent between the minimum and maximum phases.

Due to the rotational shift of the sun, our solar spectra should be shifted by ± 2 km s^{-1} between east and west, which should introduce a broadening of the line closer to the equator when we integrate the spectra. But we notice from our Table 1 that this is not the case, rather the opposite. While there exists broadening due to shifting post-integration, we surmise that the effects of such shifts are quite low due to the magnitudes of the velocities of shifting, as compared to activities that take place. To visualize this, we have plotted a LW comparison plot between the active and quiet phases in Fig. 7. We have chosen and averaged about 7–10 d each in the months of 2020

Table 1. Mean and standard deviations for the LW variations of the parameters.

Latitude (°)	Quantified variations of various Ca-K line parameters				
	K_1 Width (Å)	K_2 Width (Å)	K_3 Intensity (Normalized)	K_{2v}/K_{2r} Intensity ratio	K_{2v}/K_3 Intensity ratio
−70	0.739 ± 0.042	0.462 ± 0.030	0.062 ± 0.012	1.048 ± 0.021	1.425 ± 0.126
−60	0.690 ± 0.036	0.431 ± 0.022	0.061 ± 0.012	1.056 ± 0.022	1.426 ± 0.119
−50	0.650 ± 0.029	0.409 ± 0.015	0.060 ± 0.012	1.061 ± 0.022	1.412 ± 0.122
−40	0.625 ± 0.029	0.397 ± 0.014	0.061 ± 0.012	1.062 ± 0.023	1.387 ± 0.114
−30	0.617 ± 0.037	0.389 ± 0.016	0.063 ± 0.012	1.061 ± 0.023	1.362 ± 0.108
−25	0.624 ± 0.049	0.382 ± 0.020	0.065 ± 0.013	1.058 ± 0.023	1.337 ± 0.105
−20	0.627 ± 0.055	0.377 ± 0.019	0.066 ± 0.013	1.058 ± 0.024	1.326 ± 0.102
−15	0.622 ± 0.057	0.375 ± 0.022	0.066 ± 0.014	1.058 ± 0.023	1.320 ± 0.101
−10	0.613 ± 0.054	0.374 ± 0.021	0.066 ± 0.014	1.059 ± 0.024	1.322 ± 0.102
−5	0.600 ± 0.048	0.377 ± 0.022	0.065 ± 0.014	1.060 ± 0.023	1.322 ± 0.105
0	0.591 ± 0.037	0.379 ± 0.024	0.065 ± 0.014	1.061 ± 0.023	1.323 ± 0.105
5	0.595 ± 0.039	0.377 ± 0.022	0.065 ± 0.013	1.060 ± 0.023	1.320 ± 0.103
10	0.606 ± 0.047	0.377 ± 0.023	0.066 ± 0.013	1.059 ± 0.023	1.317 ± 0.101
15	0.618 ± 0.054	0.375 ± 0.022	0.066 ± 0.013	1.057 ± 0.023	1.317 ± 0.100
20	0.627 ± 0.060	0.376 ± 0.022	0.067 ± 0.013	1.056 ± 0.022	1.318 ± 0.098
25	0.629 ± 0.059	0.379 ± 0.019	0.066 ± 0.013	1.056 ± 0.023	1.326 ± 0.101
30	0.624 ± 0.054	0.385 ± 0.019	0.065 ± 0.013	1.057 ± 0.023	1.334 ± 0.104
40	0.622 ± 0.046	0.390 ± 0.017	0.064 ± 0.013	1.057 ± 0.023	1.348 ± 0.109
50	0.629 ± 0.031	0.399 ± 0.015	0.062 ± 0.012	1.058 ± 0.021	1.373 ± 0.111
60	0.657 ± 0.029	0.415 ± 0.017	0.062 ± 0.012	1.055 ± 0.020	1.386 ± 0.115
70	0.704 ± 0.038	0.440 ± 0.024	0.065 ± 0.012	1.044 ± 0.021	1.367 ± 0.118

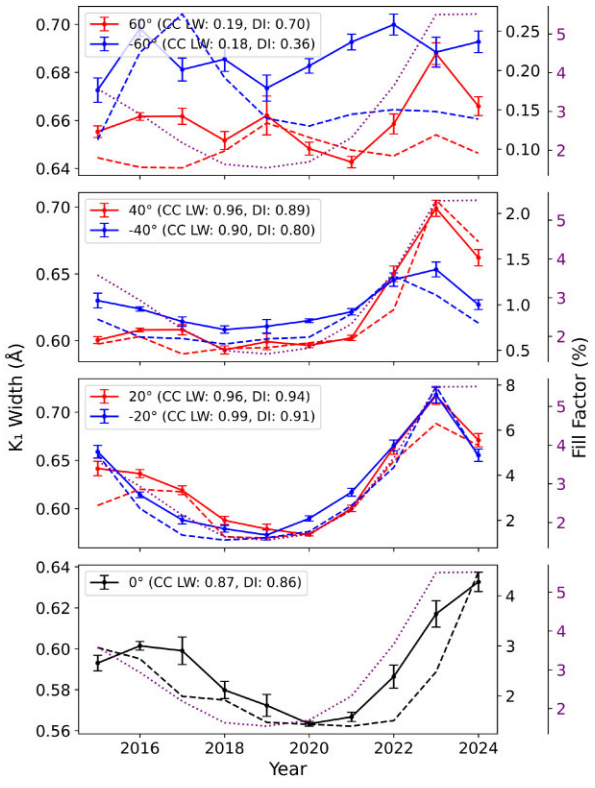

Figure 5. Temporal variations in K_1 widths for select latitudes. The circular points with error bars show the yearly averaged widths, red for northern latitudes and blue for southern. The red and blue (black for 0°) dashed lines show the yearly averaged LW plage + spot FF for the respective hemispheres. The purple dotted line shows the yearly averaged DI FF.

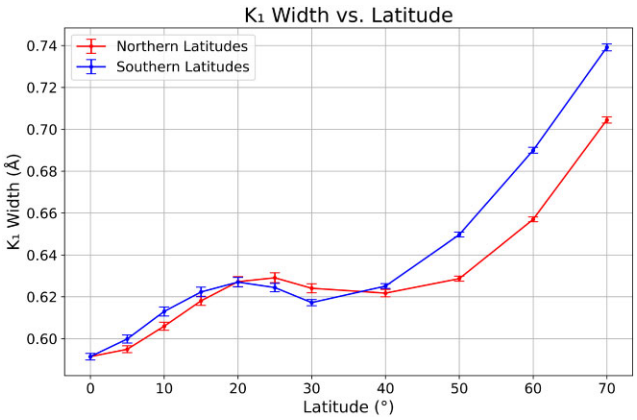

Figure 6. Time-averaged K_1 width variation as a function of latitude. Northern hemisphere in red and Southern hemisphere in blue.

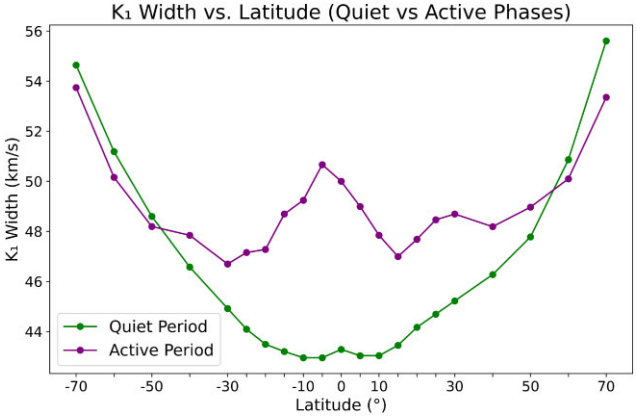

Figure 7. K_1 width variations as a function of latitude during quiet (green) and active (purple) phases of the sun.

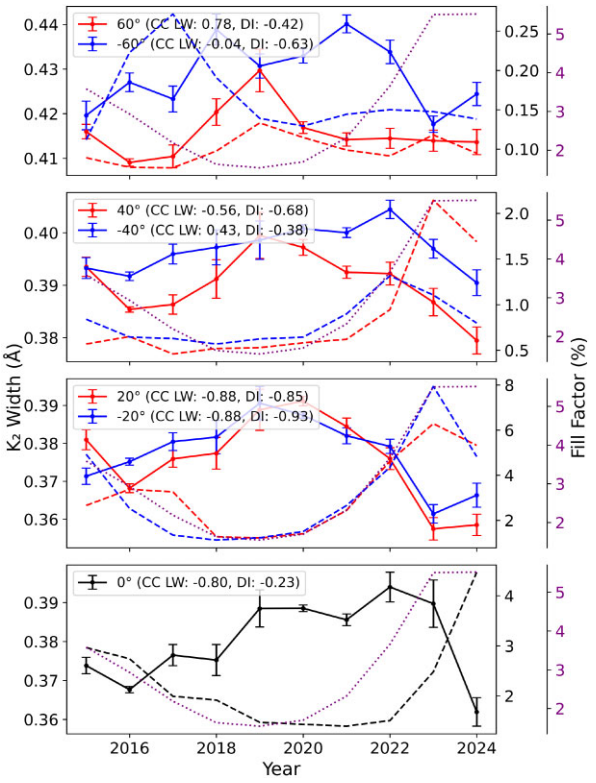

Figure 8. Temporal variations in K_2 widths for select latitudes. The circular points with error bars show the yearly averaged widths, red for northern latitudes and blue for southern. The red and blue (black for 0°) dashed lines show the yearly averaged LW plage + spot FF for the respective hemispheres. The purple dotted line shows the yearly averaged DI-FF.

February and 2024 February where the number of sunspots (proxy for activities) were all 0 and greater than 100, respectively.

3.2 Variations in K_2 widths

Fig. 8 shows the variations in the K_2 widths for select latitudes over time. Most of the latitudes plotted show a similar underlying trend, which is an increase in the widths during 2015–2019/2020, followed by a decrease towards 2024, except latitudes 0° and −40°, which show an increase in the widths until 2022 before decreasing. The CCs between the K_2 width and LW-FF as well as DI-FF are negative. The maximum LW- and DI-FF negative correlations of −0.88 and −0.93 both are obtained at 20°S (also at 20°N for LW-FF), and minimum negative correlations of −0.04 and −0.23 are obtained at 60°S and 0° latitudes. It may be noted that despite the trend line showing a clear negative correlation, the smaller LW-FF CC at 60°S is due to a few consecutive individual data points that show a positive correlation when considered two at a time.

Fig. 9 shows the plot of K_2 width, averaged over time, as a function of latitude. The width varies in the range of 0.374–0.462 Å, with the standard deviations ranging from 0.014 to 0.030 Å. It can be seen that the K_2 width increases from the equator to the poles, with a small peak at 0°. As the trend in K_1 width, the K_2 widths are smaller in the Northern hemisphere, and the increase is steeper in the Southern hemisphere, moving from 50°S to 70°S. The averaged K_2 width over all latitudes varies by 35.26 per cent between the minimum and maximum phases.

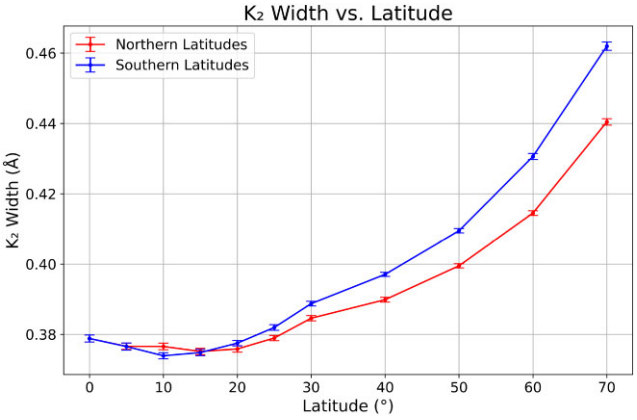

Figure 9. Time-averaged K_2 width variation as a function of latitude. Northern hemisphere in red and Southern hemisphere in blue.

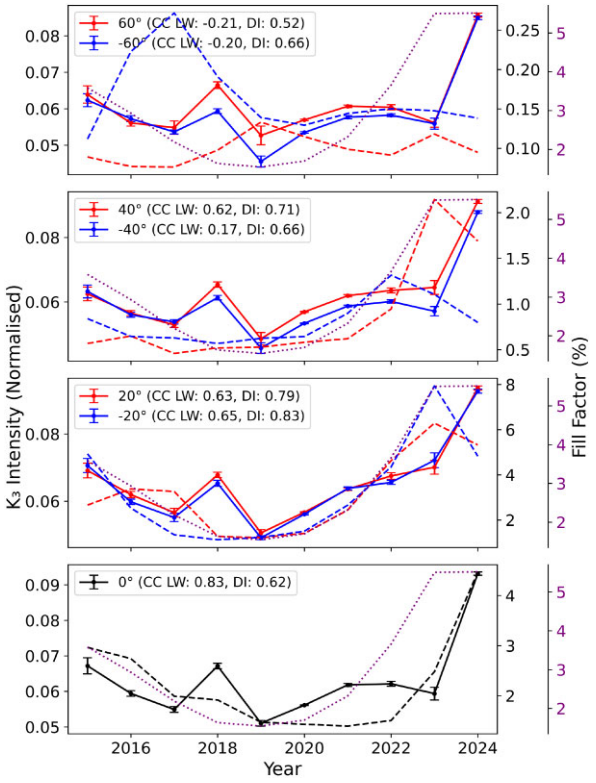

Figure 10. Temporal variations in K_3 intensities for select latitudes. The circular points with error bars show the yearly averaged intensities, red for northern latitudes and blue for southern. The red and blue (black for 0°) dashed lines show the yearly averaged LW plage + spot FF for the respective hemispheres. The purple dotted line shows the yearly averaged DI-FF.

3.3 Variations in K_3 intensities

Fig. 10 shows the variations in the K_3 intensities over the past 10 yr for select latitudes. A similar trend is seen in each of the latitudes plotted, which is a decrease in the intensities during 2015–2019/2020, followed by an increase towards 2024. The CCs between the K_3 intensity and LW-FF as well as DI-FF are mostly positive. The maximum LW- and DI-FF correlations of 0.83 and 0.83 are obtained at 0° and 20°S latitudes, and minimum correlations of 0.17 and 0.52 are obtained at 40°S and 60°N latitudes. The negative CC of LW-FF at 60° latitudes may be due to the minute noise in the data despite

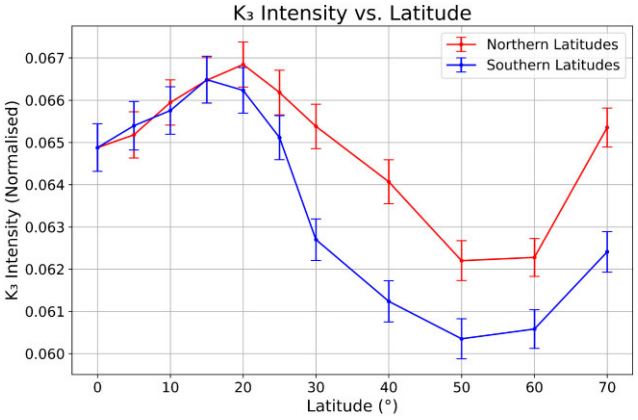

Figure 11. Time-averaged K_3 intensity variation as a function of latitude. Northern hemisphere in red and Southern hemisphere in blue.

the outlier removal. A possibility for the anomalous behaviour of the parameter plots in 2018 could be the underperformance of CCD.

Fig. 11 shows the plot of K_3 intensity, averaged over time, as a function of latitude. The intensity varies in the range of 0.060–0.067 units, with the standard deviations ranging from 0.012 to 0.014 units. The intensity variation shows an increase on either side of the 0° latitude until 20°N and 15°S, thereupon the trend falls below the intensity value at 0°, moving towards 50° on either side. From 50° on either side (with the southern side lower than the northern side), the intensity then increases again towards the poles, higher in the Northern hemisphere. The averaged K_3 intensity over all latitudes varies by 62.60 per cent between the minimum and maximum phases.

3.4 Variations in K_{2v}/K_{2r} intensity ratios

Fig. 12 shows the variations in the K_{2v}/K_{2r} intensity ratios over time for select latitudes. The intensity ratio for each of the latitudes plotted shows a similar trend, which is an increase in the ratios during 2015–2019/2020, followed by a decrease towards 2024. The CCs between the K_{2v}/K_{2r} intensity ratio and LW-FF as well as DI-FF are mostly negative. The maximum LW- and DI-FF negative correlations of −0.75 and −0.66 are obtained at 0° and 20°S (also at 40°N for DI-FF), and minimum negative correlations of −0.02 and −0.44 are obtained at 60°S and 60°N latitudes. The anomalous behaviour of the parameter plot follows the same reasoning as the K_3 intensity. The small LW-FF correlation at 60°S and the positive LW-FF correlation at 60°N may be caused due to the anomalous behaviour.

Fig. 13 shows the plot of the K_{2v}/K_{2r} intensity ratio, averaged over time, as a function of latitude. The ratio varies in the range of 1.044–1.062, with the standard deviations ranging from 0.017 to 0.020. From a central peak at 0°, the ratio falls on either side until 25°S and 20°N, whereupon the ratio rises (slightly above the ratio value at 0°, on the southern side), moving towards 40°S and 50°N. From these latitudes on either side, the ratio dips sharply towards the poles, steeper in the Northern hemisphere. The ratios in the Northern hemisphere are generally lower than those in the Southern hemisphere. The averaged K_{2v}/K_{2r} intensity ratio over all latitudes varies by 14.49 per cent between the minimum and maximum phases.

3.5 Variations in K_{2v}/K_3 intensity ratios

Fig. 14 shows the variations in the K_{2v}/K_3 intensity ratios between 2015 and 2024 for select latitudes. The intensity ratios for all latitudes show similar trends, which are an increase during 2015–2019/2020,

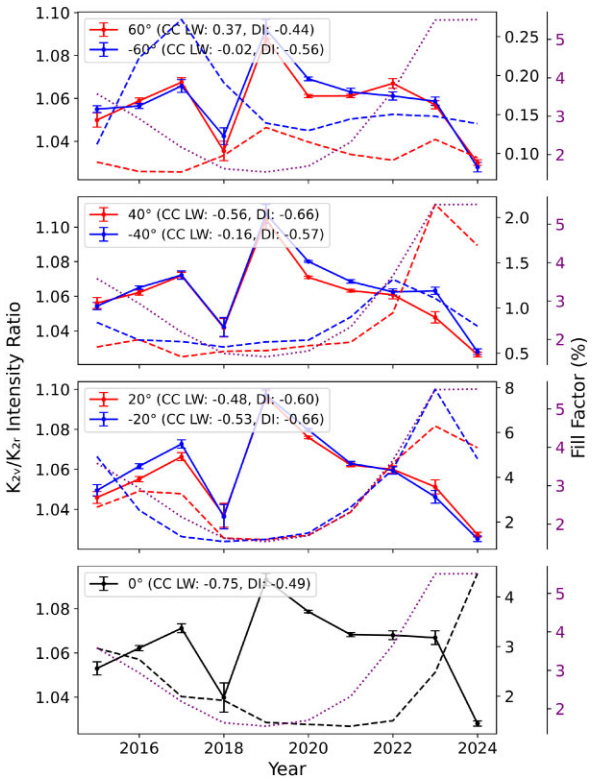

Figure 12. Temporal variations in K_{2v}/K_{2r} intensity ratios for select latitudes. The circular points with error bars show the yearly averaged intensity ratios, red for northern latitudes and blue for southern. The red and blue (black for 0°) dashed lines show the yearly averaged LW plage + spot FF for the respective hemispheres. The purple dotted line shows the yearly averaged DI-FF.

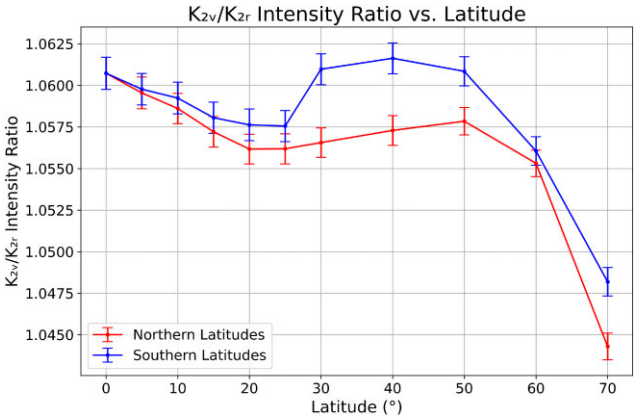

Figure 13. Time-averaged K_{2v}/K_{2r} intensity ratio variation as a function of latitude. Northern hemisphere in red and Southern hemisphere in blue.

followed by a decrease towards 2024. The CCs between the K_{2v}/K_3 intensity ratio and LW-FF as well as DI-FF are mostly negative. The maximum LW- and DI-FF negative correlations of −0.68 and −0.64 are obtained at 0° and 20°S, and minimum negative correlations of −0.15 and −0.40 are obtained at 40°S and 60°N. The anomalous behaviour of the parameter plot follows the same reasoning as the K_3 intensity. The overall small LW-FF correlation and the positive LW-FF correlation at 60° latitudes may be caused due to the anomalous behaviour.

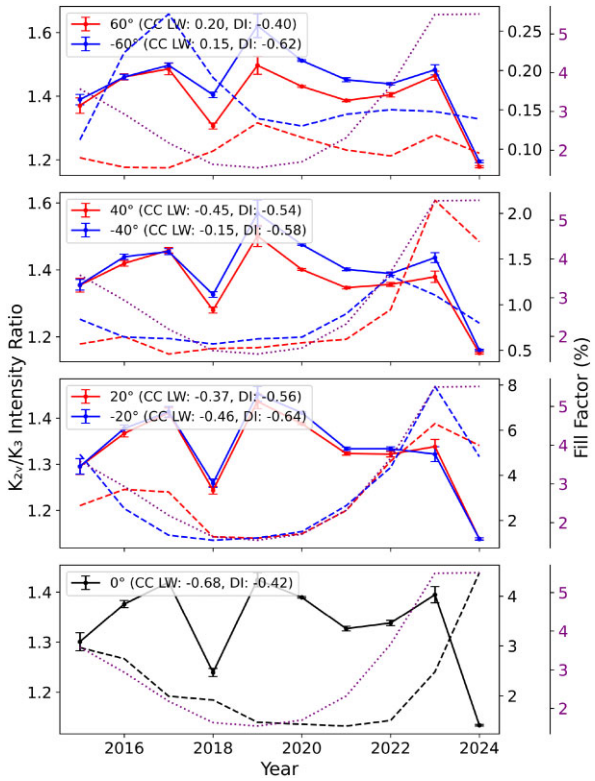

Figure 14. Temporal variations in K_{2v}/K_3 intensity ratio for select latitudes. The circular points with error bars show the yearly averaged intensity ratios, red for northern latitudes and blue for southern. The red and blue (black for 0°) dashed lines show the yearly averaged LW plage + spot FF for the respective hemispheres. The purple dotted line shows the yearly averaged DI-FF.

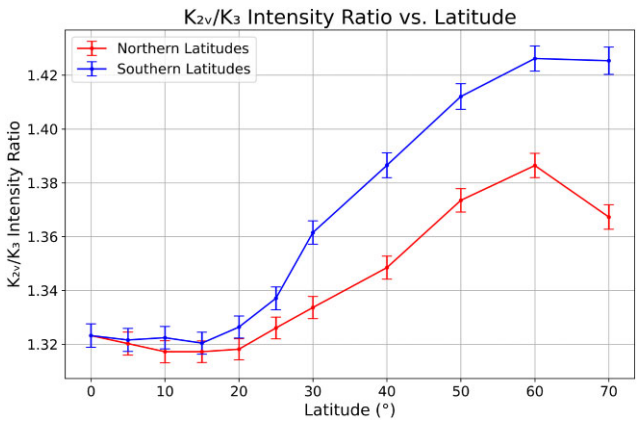

Figure 15. Time-averaged K_{2v}/K_3 intensity ratio variation as a function of latitude. Northern hemisphere in red and Southern hemisphere in blue.

Fig. 15 shows the plot of the K_{2v}/K_3 intensity ratio, averaged over time, as a function of latitude. The ratio varies in the range of 1.317–1.426, with the standard deviations ranging from 0.100 to 0.126. From a small central bump at the 0° latitude, the ratio rises on either side until 60°, thereupon, the ratio falls slightly towards the pole in the Southern hemisphere, and the ratio falls sharply towards the pole in the Northern hemisphere. The ratios in the Northern hemisphere are generally lower than those in the Southern hemisphere, and the rise in the Southern hemisphere is steeper than that in the Northern

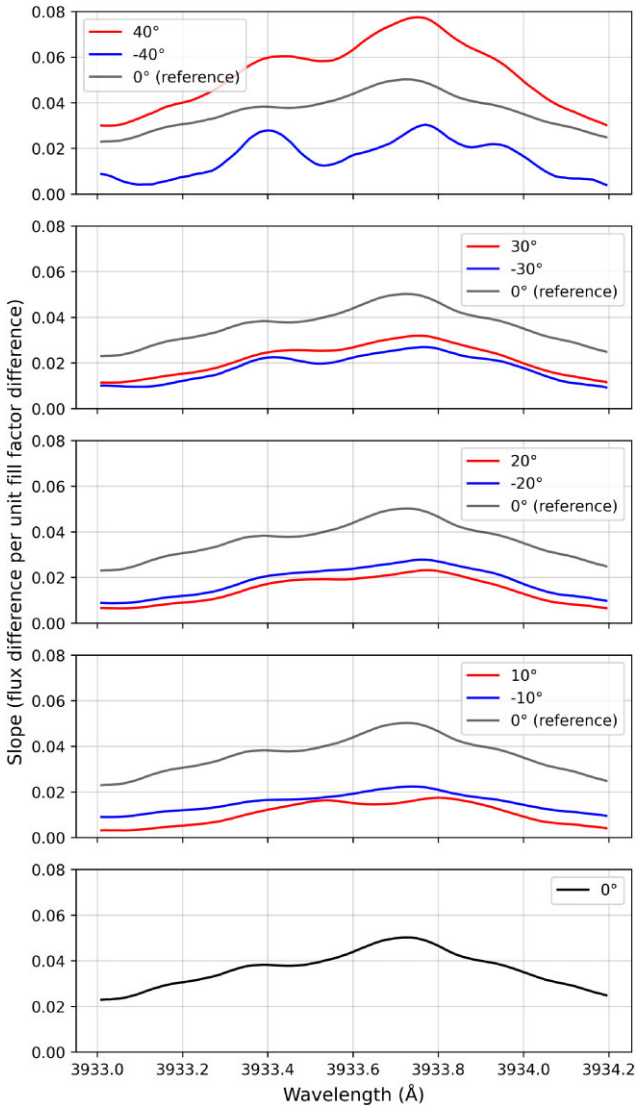

Figure 16. Flux difference per unit FF difference at various wavelengths. Northern hemisphere in red and Southern hemisphere in blue. The 0° latitude is shown as a reference with the other latitude pairs.

hemisphere. The averaged K_{2v}/K_3 intensity ratio over all latitudes varies by 36.52 per cent between the minimum and maximum phases.

3.6 Variations in flux difference per FF difference

Fig. 16 shows the flux difference per unit FF difference at wavelengths between 3933.0 and 3934.2 Å for various latitudes. All profiles exhibit positive slopes, confirming that increased magnetic FF correlates with enhanced Ca II K line intensity. Each profile displays a prominent peak near the line core (3933.6–3933.7 Å), indicating maximum sensitivity to activity changes occurs at the K_3 region. The ±40° latitude pair shows the highest peak magnitudes, with the Northern hemisphere reaching ≈0.075 and Southern hemisphere ≈0.03, demonstrating clear north–south asymmetry. The ±30° pair exhibits moderate asymmetry favouring the north with peaks of ≈0.032 (north) and ≈0.027 (south). The ±20° pair displays reversed asymmetry with the Southern hemisphere dominant at ≈0.028 compared to the Northern hemisphere's ≈0.023. The ±10° pair shows the Southern hemisphere reaching ≈0.023, while the

Northern hemisphere peaks at ≈0.017. The equatorial belt (0°) shows an intermediate value of ≈0.05. The north–south asymmetries vary systematically with latitude, indicating latitude-dependent magnetic activity patterns during our observation period.

4 DISCUSSION

The variations in K_1 and K_2 widths of the Ca-K line profile can provide insights into the magnetic field variations and activity of the sun (Bertello et al. 2016). The increase in temperature with height in the sun's chromosphere causes an increase in the widths of the Ca-K lines with latitude, which is seen as we move from the equator to the poles (Smith 1960; Engvold 1966; Pietrow et al. 2023). This relationship highlights the non-uniformity of solar activity across latitudes, indicating that magnetic field strengths and temperatures vary significantly, which is important for understanding solar dynamics and predicting solar phenomena (McIntosh et al. 2015). Another possibility could be due to increasing optical depth as we move towards the poles. Further, the K_1 width of the Ca-K line increases with solar activity, likely due to the higher temperature of active regions causing broadening of the Ca-K profile. Conversely, the K_2 width decreases with increasing solar activity. These findings emphasize the importance of monitoring these widths as indicators of solar activity levels and magnetic field variations. This has been previously reported by White & Livingston (1981), Sivaraman et al. (1987), and Sindhuja & Singh (2015). Cretignier et al. (2024) report their observations for the Meudon spectroheliogram data cubes, where they found the emission profiles to be thinner in the sunspot areas compared to plage areas, though they remarked that the result may not be universal. These trends are observed towards the 15–20° latitudes on both hemispheres, as depicted by the width plots in Figs 6 and 9, suggesting activities in those regions. These variations are not only significant for understanding solar dynamics but also hold the potential for improving space weather prediction models (Temmer 2021).

Increased K_3 intensity suggests a higher abundance of calcium ions in the solar atmosphere (Grigoryeva, Ozhogina & Teplitskaya 2000). Changes in the K_3 intensity from the equator to the poles can unveil latitudinal dependencies, as these variations in intensity could reflect the variations in solar activity across latitudes. Comparing with K_1 and K_2 widths, we see a correlated trend with K_3 intensity in Fig. 11, where the intensity increases towards the 15–20° latitudes on both hemispheres, again suggesting activities in those areas, whereas the decrease in the intensity between 20° and 50° on either hemisphere may point to fewer activities occurring in these latitudes. This asymmetry between hemispheres may provide insights into underlying mechanisms driving hemispheric solar activity (Norton et al. 2014). Further, the increase in intensity beyond these minima may be due to higher temperatures in the polar regions as compared with equatorial regions (Das & Abhyankar 1955; Beckers 1960; Plaskett 1966). The higher intensity in the Northern hemisphere suggests a higher amount of activity. This suggests that monitoring calcium ion abundance can serve as an effective proxy for assessing regional solar activity.

The K_{2v}/K_{2r} intensity ratio provides the comparison of the violet (K_{2v}) and red (K_{2r}) components of the K_2 peaks in the Calcium-K spectrum. Changes in this ratio primarily reflect velocity fields in the chromosphere, with asymmetries largely resulting from Doppler shifts (Grossmann-Doerth, Kneer & von Uexküll 1974; Cram & Dame 1983). The presence of upward-propagating acoustic shocks in the chromosphere tends to enhance emission in the violet wing (K_{2v}) relative to the red wing (K_{2r}), producing profiles with $K_{2v}/K_{2r} > 1$ in most observations (Carlsson & Stein 1997). This asymmetry emerges because shocks create large velocity gradients that shift the absorption profiles of material behind the shock towards shorter wavelengths, reducing opacity on the violet side of the line, while increasing it on the red side (Carlsson & Stein 1997). Bappu & Sivaraman (1971) suggest that changes in the K_3 intensity can cause variations in the K_{2v} and K_{2r} intensities and that higher absorption (the K_3 core) may result in a decrease in K_{2v} intensity compared to K_{2r} intensity. Understanding this ratio may be important for interpreting chromospheric dynamics and linking them to broader magnetic activity patterns. We observe that the peaks and dips of the K_{2v}/K_{2r} intensity ratio in Fig. 13 correspond to the dips and peaks of K_3 intensity in Fig. 11. These figures confirm the above-mentioned suggestion by Bappu & Sivaraman (1971).

The K_{2v}/K_3 intensity ratio reveals information about the relative strength of the emissions from the lower chromosphere and the upper chromosphere (White et al. 1998, Singh 1988). An increased K_{2v}/K_3 ratio might suggest enhanced temperatures or specific conditions leading to stronger violet emission relative to the overall intensity at the K_3 central minimum. This finding emphasizes how temperature gradients influence chromospheric emissions, contributing to our understanding of solar atmospheric structure. These temperature gradients may also reflect changes in the magnetic field structure, which could be important for future magnetic reconstructions of the solar atmosphere (Lagg et al. 2017). From Fig. 15, we can observe that the overall trend of the K_{2v}/K_3 intensity ratio increases from the equator to the poles. As suggested earlier, the temperatures in the polar regions are higher compared to equatorial regions. The K_{2v} line is stronger at higher temperatures, whereas the K_3 line represents the absorption core in cooler regions.

The K_1 and K_2 widths of the Ca-K line profiles have temporal variations that are dependent on the solar cycle. The K_1 width increases/decreases towards the solar maximum/minimum, whereas the K_2 width decreases/increases. These trends are apparent from Figs 5 and 8. The 20° latitudes on both hemispheres display larger K_1 width variations in comparison to the other latitudes as more activities occur around the 20° belt. This is due to the equatorial drift of the sunspots from around 40° to the equator. The sunspots being magnetic activities contribute to the increased K_1 widths. The variations at 40° and the equator are lower than the latitudes in between. This is because the number of sunspots is lower when the cycle starts around 40° latitudes. It then increases as the cycle progresses with the sunspots drifting towards the equator and finally reduces as the spots approach the equator. The strong positive correlations between K_1 width and both plage and spot FFs (with maximum correlations of 0.95 and 0.96 at 20°N and 40°N, respectively) confirm that this parameter is directly influenced by magnetic activity. The notably weaker correlations at high latitudes (minimum of 0.35 and 0.33 at 60°S) align with expectations from the Butterfly diagram pattern, where active regions are concentrated between ±40° latitude and migrate equatorwards as the cycle progresses. As with the K_1 width, the K_2 width displays larger variations in the 20° latitudes than those in the other latitudes. Interestingly, K_2 width shows strong negative correlations with both plage and spot FFs (maximum negative correlations of −0.93 and −0.90 at 20°S), indicating an inverse relationship with surface magnetic activity. As the solar cycle progresses, the activities increase, leading to an increase in the intensities with the magnetic field strengths. This may have contributed to the smaller K_2 widths towards the solar maximum and larger widths towards the solar minimum. The weaker correlation at the equator (minimum negative correlations of –0.21 and –0.05) suggests that this parameter may be influenced by additional factors beyond simple active region presence. Further, this indicates that

specific latitudinal bands are more sensitive to changes in solar activity, which is critical for modelling solar cycles and predicting related phenomena. Continued study of these latitudinal variations could help refine our understanding of the relationship between magnetic activity and the solar cycle (Hathaway 2015).

The K_3 intensities of the Ca-K line profiles also have temporal variations that follow the solar cycles (Fig. 10). The K_3 intensity increases/decreases towards the solar maximum/minimum. This parameter shows consistent positive correlations with both plage and spot FFs across all latitudes (maximum correlations of 0.81 and 0.73 at 20°S), confirming that K_3 intensity directly responds to the presence of magnetic activity. As the activities increase, the energy released increases, and thus, the observed intensity increases. In contrast, as seen in the LW variations, the K_{2v}/K_{2r} (Fig. 12) and K_{2v}/K_3 (Fig. 14) intensity ratios show the opposite behaviour to the K_3 intensity. That is, the ratios increase/decrease towards the solar minimum/maximum. The anomalous behaviour observed in 2018, particularly in the intensity and their ratio parameters, is not clearly understood. One possibility could be the underperformance of CCD. These observations highlight the intricate relationships between different emissions and their dependence on solar cycle phases, emphasizing their importance for in-depth modelling efforts.

When analysing our data in the context of the Butterfly diagram, we observe that the strongest correlations between line profile parameters and magnetic activity indicators (plage and spot FFs) consistently appear within ±40° latitude, which precisely corresponds to the active region belt where the Butterfly pattern manifests. The temporal evolution of these correlations further supports this connection, with signals at higher latitudes (e.g. 40°N) being more pronounced during the ascending phase of the cycle, consistent with the polewards migration of active regions. The weakening correlations beyond ±40° latitude is due to the lack of spots and plages in these regions.

As expected, the plage and spot CCs for each parameter confirm these temporal behaviours. In each parameter, the solar cycle dependence appears to be stronger between 20°N and 20°S, slightly weaker towards 40°N and 40°S, and weakest towards the poles (with CCs of K_2 width and K_{2v}/K_3 intensity ratio at 60°S as exceptions). Generally, the correlations seem to be weaker in the Northern hemisphere than in the Southern hemisphere, except for the K_1 width and the 40° belts of K_2 width, the K_3 intensity, and the K_{2v}/K_{2r} intensity ratio, where Northern hemisphere correlations are stronger. This hemispheric asymmetry in correlation strength may indicate fundamental differences in magnetic field evolution between the Northern and Southern hemispheres during this phase of the solar cycle. For each parameter, except for the K_1 width, the 20°S latitude shows the highest correlations compared to other latitudes. The plage and spot CCs for K_1 width at 20°S are 0.92 each, whereas those of 20°N are 0.95 each, despite which our observation that the 20°S latitudes show the highest correlation holds true. Further, in terms of absolute CCs, K_1 width shows higher correlations than other parameters. The particularly strong correlations between K_1 width and magnetic activity indicators suggest that this parameter may serve as the most reliable chromospheric proxy for tracking solar magnetic activity evolution. This information may be important for developing predictive models regarding solar behaviour and its implications for space weather.

The segmentation of SDO data to extract sunspot and plage FFs has proven valuable in quantifying the relationship between our spectral parameters and surface magnetic features. The strong latitude-dependent correlations confirm that variations in Ca-K line profiles are directly linked to the changing distribution of active regions over the solar cycle, rather than being merely coincidental with the sunspot number trend. The FF analysis particularly reveals how the type and coverage of magnetic features at different latitudinal bands influence specific spectral parameters in distinct ways, providing a more mechanistic understanding of the observed variations beyond simple cycle-dependent correlations.

Previous work by Sivaraman et al. (1987) showed the temporal variations in K_3 intensity and the intensity ratios of K_{2v}/K_3 and K_{2v}/K_{2r} between the years 1968 and 1984. Sindhuja (2015) obtained the temporal variations in K_1 and K_2 widths as well as the latitudinal variations (during quiet and active phases) for all five parameters between the years 1989 to 2011. The results from our study conform to the trends seen historically in their work. This consistency supports the reliability of these trends over multiple solar cycles, suggesting that these parametric variations are persistent features of solar activity. Such agreement highlights the importance of continued observations to deepen our understanding of these long-term solar behaviours. Future comparisons with additional data sets could help validate these findings over even longer periods, strengthening our models of solar behaviour (Chatzistergos et al. 2020).

The slope profiles in Fig. 16 represent the mean spectral response of the chromosphere to magnetic activity, effectively showing how the Ca II K line shape changes when active regions are added to a quiet Sun background. The consistent peak near the K_3 line core reflects the well-established behaviour where active regions fill in and brighten the central reversal, attributed to enhanced temperatures in the upper chromosphere of magnetic features (Shine & Linsky 1974). The latitude dependence of these profiles likely reflects the combination of several factors, such as the intrinsic distribution of active regions over the solar cycle, centre-to-limb viewing effects that systematically affect different latitude bands, and potential variations in the magnetic field properties at different latitudes. The methodology follows similar approaches described by Cretignier et al. (2024), who noted that such latitude-dependent intensity profiles inherently include centre-to-limb variation effects on active region emission. The hemispheric differences observed in our data period (2015–2024), which spans the transition from Solar Cycle 24 to 25, reflect the latitude-dependent activity patterns characteristic of this phase of the solar cycle. The spectrally resolved approach provides more detailed information than traditional line indices, complementing our findings that K_1 width correlates with FF by the precise mapping of wavelengths that drive these correlations.

5 CONCLUSION

We obtained observations of the Ca-K line profiles of the sun for a period of about 10 yr from 2015 to 2024 at the KSO. From these line profiles, we have extracted the K_1 width, K_2 width, K_3 intensity and the intensity ratios of K_{2v}/K_{2r} and K_{2v}/K_3 as functions of latitude and time. As we move towards the polar regions, the time-averaged K_1 and K_2 widths and intensity ratio of K_{2v}/K_3 increase, whereas the time-averaged K_3 intensity and intensity ratio of K_{2v}/K_{2r} decrease. The parameters K_1 width and K_3 intensity show peaks around 15–20° on both hemispheres, whereas K_2 width and the intensity ratios of K_{2v}/K_{2r} and K_{2v}/K_3 show dips around those latitudes. Generally, the trends indicate that the activity regions are mostly found between 40°S and 40°N. Finally, the yearly averaged temporal variation plots show that the K_1 width and K_3 intensity increase/decrease with solar maximum/minimum, whereas the K_2 width and the intensity ratios of K_{2v}/K_{2r} and K_{2v}/K_3 show decrease/increase. These temporal behaviours are further confirmed by the correlation coefficients between the parameters and the plage and spot FFs. Our results are also in agreement with the previous spatial and temporal studies between 1986 and 2011. Additionally, we derived slope profiles representing the spectral response of the Ca II K line to changes

in magnetic FF across different latitudes. These profiles consistently peak near the K_3 line core, confirming that the primary spectral signature of solar activity occurs through filling-in of the central reversal. The profiles also show north–south differences that vary with latitude. Further studies are on the anvil to understand the full significance of the results.

CONFLICT OF INTEREST

The authors declare no conflict of interest.

ACKNOWLEDGEMENTS

The authors gratefully acknowledge the tireless effort of the KSO team to obtain the spectral data and the IIA scientists for developing the calibration techniques for the data. This research has made use of data from the HMI instrument onboard the SDO, a mission for NASA's Living With a Star program. The authors acknowledge the use of the SOLASTER[1] Python package for data analysis. Some of the authors also express their gratitude to The Chancellor of Amrita Vishwa Vidyapeetham for their support. This work is funded by the Department of Science and Technology, Government of India.

DATA AVAILABILITY

The raw Ca II K spectral data are available on request at the Indian Institute of Astrophysics. HMI data used in this study are courtesy of NASA/SDO and the AIA, EVE, and HMI science teams, and the data are publicly available from the JOINT SCIENCE OPERATIONS CENTER[2] (JSOC) at Stanford University. The Mg II index data are available from the UVSAT GROUP[3] of the University of Bremen.

REFERENCES

Bappu M. K. V., Sivaraman K. R., 1971, Sol. Phys., 17, 316
Beckers J. M., 1960, Bull. Astron. Inst. Neth., 15, 85
Bertello L., Pevtsov A. A., Ulrich R. K., 2020, ApJ, 897, 181
Bertello L., Pevtsov A., Tlatov A., Singh J., 2016, Sol. Phys., 291, 2967
Carlsson M., Stein R. F., 1997, ApJ, 481, 500
Charbonneau P., 2020, Living Rev. Sol. Phys., 17, 4
Chatzistergos T. et al., 2020, A&A, 639, A88
Chatzistergos T., Krivova N. A., Ermolli I., 2022, Front. Astron. Space Sci., 9, 336
Cram L. E., Dame L., 1983, ApJ, 272, 355
Cretignier M., Pietrow A. G. M., Aigrain S., 2024, MNRAS, 527, 2940
Das A. K., Abhyankar K. D., 1955, Vistas Astron., 1, 658
Engvold O., 1966, Astrophys. Norv., 10, 101
Ervin T. et al., 2022, Astrophysics Source Code Library, record ascl:2207.009
Froehlich C., Foukal P. V., Hickey J. R., Hudson H. S., Willson R. C., 1991, in Sonnett C. P., Giampa M. S., Matthews M.S., eds, The Sun in Time. University of Arizona Press, Tucson, p. 11
Fröhlich C., Lean J., 1998, Geophys. Res. Lett., 25, 4377
Gray L. J. et al., 2010, Rev. Geophys., 48, RG4001
Grigoryeva S. A., Ozhogina O. A., Teplitskaya R. B., 2000, Sol. Phys., 195, 269
Grossmann-Doerth U., Kneer F., von Uexküll M., 1974, Sol. Phys., 37, 85
Hale G. E., Ellerman F., 1904, ApJ, 19, 41
Hathaway D. H., 2015, Living Rev. Sol. Phys., 12, 4
Keil S. L., Worden S. P., 1984, ApJ, 276, 766
Lagg A., Lites B., Harvey J., Gosain S., Centeno R., 2017, Space Sci. Rev. , 210, 37
Makarov V. I., Tlatov A. G., 2000, Astron. Rep., 44, 759
McIntosh S. W. et al., 2015, Nat Commun., 6, 6491
Morrill J. S., Floyd L., McMullin D., 2011, Sol. Phys., 269, 253
Nindos A., Zirin H., 1998, Sol. Phys., 179, 253
Norton A. A., Charbonneau P., Passos D., 2014, Space Sci. Rev., 186, 251
Oranje B. J., 1983, A&A, 124, 43
Ortiz A., Rast M., 2005, Mem. Soc. Astron. Ital., 76, 1018
Pap J. M., Floyd L., Lee R. B., Parker D., Puga L., Ulrich R., Varadi F., Viereck R., 1997, in Wilson. A., ed., ESA SP-415: Long-Term Variations in Total Solar and UV Irradiances. ESA, Noordwijk, p. 251
Pietrow A. G. M., Kiselman D., Andriienko O., Petit dit de la Roche D. J. M., Díaz Baso C. J., Calvo F., 2023, A&A, 671, A130
Plaskett H. H., 1966, MNRAS, 131, 407
Priyal M., Singh J., Ravindra B., Sindhuja G., 2023, ApJ, 944, 218
Shine R. A., Linsky J. L., 1974, Sol. Phys., 39, 49
Sindhuja G., 2015, PhD Thesis, Indian Institute of Astrophysics
Sindhuja G., Singh J., 2015, JA&A, 36, 81
Sindhuja G., Singh J., Ravindra B., 2014, ApJ, 792, 22
Singh J., 1988, Kodaikanal Obs. Bull., 9, 159
Sivaraman K. R., Singh J., Bagare S. P., Gupta S. S., 1987, ApJ, 313, 456
Smith E. V. P., 1960, ApJ, 132, 202
Snow M., Weber M., Machol J., Viereck R., Richard E., 2014, JSWSC, 4, A04.
Solanki S. K., Krivova N. A., Haigh J. D., 2013, ARA&A, 51, 311
Temmer M., 2021, Living Rev. Sol. Phys, 18, 4
Vernazza J. E., Avrett E. H., Loeser R., 1981, ApJS, 45, 635
White O. R., Livingston W. C., 1981, ApJ, 249, 798
White O. R., Livingston W. C., Keil S. L., Henry T. W., 1998, in Balasubramaniam K. S., Harvey J., Rabin D., eds, ASP Conf. Ser. Vol. 140, Synoptic Coronal Temperature; Magnetic Field and He 11083 NM Observations. Astron. Soc. Pac., San Francisco, p. 293
White O. R., Livingston W., 1978, ApJ, 226, 679
White O. R., Suemoto Z., 1968, Sol. Phys., 3, 523
Worden J., Harvey J., 2000, Sol. Phys., 195, 247

APPENDIX A: CDF DISTRIBUTIONS

Fig. A1 shows the cumulative distributions of the line-of-sight velocity (v) and centre-to-limb angle ($\mu = \cos\theta$). The cumulative distributions of v show how the rotational velocities are distributed across latitude bands and that the range of velocities decreases from 2 km s^{-1} at 0° latitude to 1 km s^{-1} at 60° latitude. The cumulative distributions of μ show the projection effect as we move from the centre of the solar disc.

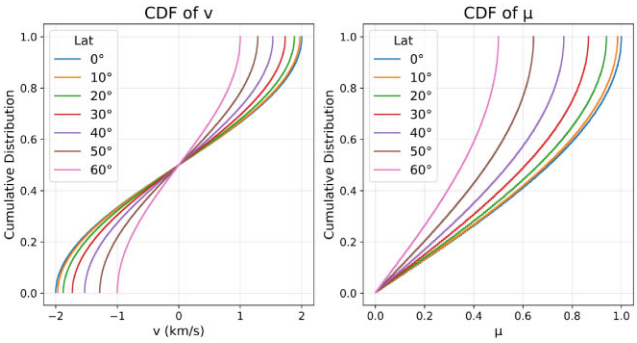

Figure A1. Cumulative distribution plots of (left) v and (right) μ for various latitudes.

This paper has been typeset from a TEX/LATEX file prepared by the author.

[1]https://github.com/tamarervin/SolAster
[2]http://jsoc.stanford.edu/
[3]https://www.iup.uni-bremen.de/UVSAT/